Additive Manufacturing 28 (2019) 228–235

Contents lists available at ScienceDirect

Additive Manufacturing

journal homepage: www.elsevier.com/locate/addma

Full Length Article

Reducing residual stress by selective large-area diode surface heating during laser powder bed fusion additive manufacturing

John D. Roehling[a,*,1], William L. Smith[b,1], Tien T. Roehling[a], Bey Vrancken[a], Gabriel M. Guss[c], Joseph T. McKeown[a], Michael R. Hill[d], Manyalibo J. Matthews[a]

[a] Materials Science Division, Lawrence Livermore National Laboratory, 7000 East Avenue, Livermore, CA 94550, USA
[b] Materials Engineering Division, Lawrence Livermore National Laboratory, 7000 East Avenue, Livermore, CA 94550, USA
[c] Laser Systems Engineering Operations, Lawrence Livermore National Laboratory, 7000 East Avenue, Livermore, CA 94550, USA
[d] Mechanical Engineering Department, One Shields Ave, University of California, Davis, Davis, CA 95616, USA

ARTICLE INFO

Keywords:
Residual stress
Microstructure
Annealing
In situ

ABSTRACT

High residual stresses are typical in additively manufactured metals and can reach levels as high as the yield strength, leading to distortions and even cracks. Here, an in situ method for controlling residual stress during laser powder bed fusion additive manufacturing was demonstrated. By illuminating the surface of a build with homogeneously intense, shaped light from a set of laser diodes, the thermal history was controlled thereby reducing the residual stress in as-built parts. 316L stainless steel bridge-shaped parts were built to characterize the effect of in situ annealing on the residual stress. A reduction in the overall residual stress value of up to 90% was realized without altering the as-built grain structure (no grain growth). Some annealing effects on the cellular-dendritic solidification structure (patterns of higher solute content) occurred in areas that experienced prolonged exposure to elevated temperature. A comparison of the in situ process to conventional post-build annealing demonstrated equivalent stress reduction compared to rule-of-thumb thermal treatments. Use of this method could reduce or remove the need for post processing to remove residual stresses.

1. Introduction

The continual influx of metal additive manufacturing (AM) processes into the industrial space has driven the need to reduce risk. Additively manufactured parts can fail during the building stage and typically have large part-to-part variability, which can reduce service life due to defects and uncertainties in long-term properties [1–3]. Growing efforts are currently underway to qualify and certify AM parts, reducing the risk of part failure during both service and the build process. These efforts largely aim at in situ monitoring for defect detection and/or tracking, especially in the laser powder bed fusion (LPBF) process [4–6]. Monitoring would enable the location and characterization of defects as they occur, effectively implementing in situ quality control. Parts could be accepted immediately after the build, scrapped, or sent for a repair process, such as hot isostatic pressing, without further inspection.

A significant risk for additively manufactured parts, and the focus of this work, is the build-up of residual stress. The high temperature gradients inherent in the AM process can introduce particularly large residual stresses [7–12]. Residual stresses can result in deformation and distortions, and in some extreme cases, can cause cracking of parts or even build plates. Mitigating the residual stress and its effects is therefore paramount to improve the quality of as-built parts, and further enable the implementation of in situ quality control.

Residual stresses are created in thermal processes through the non-uniform plastic yielding (deformation) of material from thermal expansion. The resulting deformation in AM processes can be quite significant due to the large temperature gradients. During the build-up of residual stress in LPBF, there is an interplay between the softening and simultaneous expansion of hot material and the hardening and contraction of cold material. Solidification and subsequent shrinkage of the melt pool also play a significant role. Consequently, there are two mechanisms that contribute to the creation of residual stress. The first, which does not consider melting or addition of material and is leveraged in forming techniques such as laser bending, works as follows:

i As the metal affected by the heat source is heated, it expands and concurrently softens (the yield strength decreases). At the same

* Corresponding author.
E-mail address: roehling1@llnl.gov (J.D. Roehling).
[1] These authors contributed equally to this work.

https://doi.org/10.1016/j.addma.2019.05.009
Received 26 January 2019; Received in revised form 4 April 2019; Accepted 6 May 2019
Available online 06 May 2019

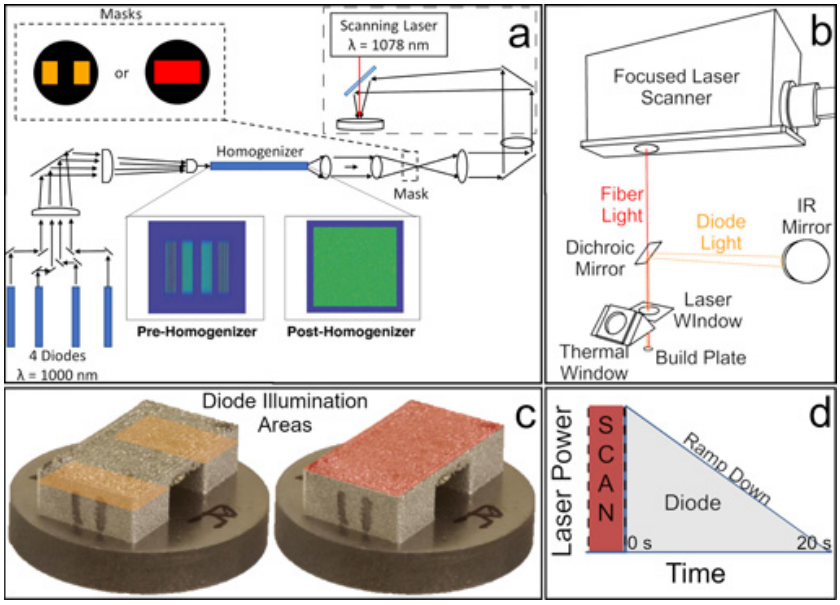

Fig. 1. a) Schematic of the diode annealing system. b) Detailed line drawing of the dotted line in a), showing the laser scanner and dichroic mirror in proximity to the build plate. c) Image of the bridges attached to 1 inch build plates that were built for the study, superimposed with the two mask shapes that were used. d) Diagram showing the diode-annealing process in time and the ramp down of diode power.

time, the surrounding metal is cooler and stronger (higher yield strength), resisting the expanding hot metal.

ii The differential expansion induces stresses in the hot region that are greater than its local, at-temperature yield strength, causing plastic deformation and compressive strain. The cooler region can sustain higher stresses, as its yield strength is higher.

iii As the hot and plastically compressed material cools, it contracts, but is constrained by the stronger and cooler surrounding regions, converting the compressive stress to tensile stress, and balanced by compressive stress in the cooler material [13].

iv The second mechanism is similar to the first, but with the addition of material on the top surface. Tensile stresses are produced in the most recently deposited material, with compressive stresses produced in the underlying material.

Therefore, if a material could be heated and cooled in the absence of temperature gradients, no residual stresses would result. Likewise, purely elastic material would not retain any residual stresses. But in practice, residual stresses can be minimized by heating and cooling with the smallest temperature gradient possible, which is challenging in AM because of the use of localized heat sources. At any given moment, the amount of *residual* stress cannot exceed the yield strength of the material. Therefore, bringing a component up to a certain temperature and cooling it sufficiently slow will reduce the residual stress to a level at or below the yield strength of the material at the treatment temperature. Residual stresses can also be annealed out of a material during post-process heat treatments through plasticity mechanisms, diffusional creep, or microplastic strain due to thermal glide [14–16].

Post-build heat treatments of LPBF parts can reduce residual stress but lead to additional processing steps/time and can alter the as-built microstructure, which may be undesirable. Moreover, post-build heat treatments do not address part distortions during the build, and any distortions will still need to be dealt with after the annealing process. Methods to reduce residual stress *during* the build are preferable. Current approaches include (1) altering the scanning strategy, [13,17–19] or (2) heating the build plate [9,20]. The first method can adjust the residual stress to some degree, but there are conflicting reports on the best scan strategy. The second method decreases in effectiveness for tall parts because of an increasing temperature drop as the distance from the build surface to the heated plate increases.

Several methods, both destructive and non-destructive, have been used for characterizing residual stresses in additively manufactured metals. The hole drilling method and the contour method rely on changing the distribution of residual stress in a part by creating stress-free surfaces (removal of material) and then calculating the residual stress distribution from the resulting deflection due to material removal [21–24]. Neutron diffraction, x-ray diffraction, and in situ digital image correlation have been used to non-destructively probe residual stresses [8,9,11,25–27]. To enable a quick and simple comparison between specimens of the same geometry, a simple beam deflection method was used here based on the bridge curvature method described by Kruth et al. [26], that measures distortion that results from mechanically releasing the stored residual stresses by cutting through support material. Though the original method relied solely on the deformation values, the use of a straight rather than curved overhang in this work allows calculation of an apparent residual stress profile from the deformation using beam theory [28,29].

In this work, an in situ annealing strategy was used to reduce residual stresses in 316L stainless steel bridges produced by LPBF. This was accomplished by a set of laser diodes selectively illuminating the recently scanned and solidified cross-section of the part with homogeneous intensity, immediately after the focused melting laser completed its scan. The strategy enabled heating/cooling cycles with small temperature gradients, resulting in a large reduction in residual stress during the build process and thereby avoiding the need for post-processing. The in situ annealing process demonstrated a residual stress reduction comparable to that of a typical furnace anneal, while causing less change to the as-built microstructure.

2. Methods

2.1. Build setup

The experimental setup is a small-scale custom LPBF machine shown in Fig. 1a,b, and is based on the work presented by Matthews et al. [30]. Four semiconductor laser diodes (1000 nm, 1.25 kW, Trumpf) are focused and combined into a homogenizer tube. The homogenizer combines the individual diode spatial profiles into an even intensity of light at the homogenizer output. Four diodes are used to achieve higher uniformity (than one diode) at the homogenizer output and subsequently at the build plate surface. This even intensity profile is then masked with two distinct patterns for building (1) the bridge supports and (2) the bridge top (i.e., supports + overhang) (Fig. 1c). The diode light is then reflected from a dichroic mirror onto

the build-plate. Illumination from a focused scanning laser (nLight, 1kW, 1078 nm fiber laser through a Nutfield 3XB scanner) passes through the dichroic to be coincident with the diode light. The illumination from the output of the homogenizer is magnified onto the build plate to be large enough to illuminate the entire 1 inch (25.4 mm) diameter build surface and is spatially shaped by the mask. The build plate is located within a customized Ar glove-box along with the powder-spreading equipment. The diode power could be controlled in any arbitrary temporal profile, up to a total of 5 kW. Custom LabView software was used to control the lasers and powder-spreader system.

The bridges were built with dimensions of 20 mm (l) × 11 mm (w) × 5 mm (h) on build plates that were 25.4 mm in diameter and 6.35 mm thick. The bridge overhang section was nominally 1.5 mm thick (30 layers). The hatch spacing was 100 μm with a 50 μm layer thickness. The focused laser beam $1/e^2$ diameter was 80 μm. A power of 250 W was chosen to minimize evaporation from the melt pool, since the proximity (15 cm) of the optical window to the build plate made the window vulnerable to metal condensate deposition. Maximum density was achieved using a scan speed of 278 mm/s and was used for all of the bridge builds (99+%, see Supplementary Data, Fig. S1). No change in density was observed between the bridges built with or without the diode annealing. The zigzag scan strategy was rotated 90° between layers, with the scanning vectors angled 45° with respect to the long axis of the bridge.

For the bridges that were annealed in situ, the diodes illuminated the bridge after the focused melting laser finished its scan (Fig. 1d). The diode light was imaged from the mask plane onto the recently scanned and solidified material while the adjacent powder was not illuminated. Diodes were initiated at full power immediately after the focused laser finished scanning, and then linearly ramped down over 20 s. Each layer was illuminated with the diode, except for the first five layers of the bridge overhang sections to avoid dross formation on the down-facing surface. The diode powers used for bridges subjected to in situ annealing were nominally 400, 800, 1000 and 1200 W (actual power was measured to be 400, 840, 1080, and 1310 W). The masks used for (1) the bridge supports and for (2) the bridge top (i.e., supports + overhang) transmitted 25.3% and 37.3%, respectively, of the maximum power.

In order to build bridge overhang sections that had acceptable down-facing surface quality, the scanning laser power was lowered and gradually increased over the first few overhanging layers [31]. The first three layers of the overhang section were built using 80 W and the fourth and fifth layers were built using 170 and 250 W, respectively. Despite heating to high temperatures, the unmelted powder surrounding the bridges (and beneath the bridge section) was unaffected (i.e., no sintering or discoloration was observed).

A FLIR A6230 thermal camera was used for temperature measurements through a 3-mm thick anti-reflective ZnSe window (Fig. 1b). This was used to measure both the spatial and time-dependent temperature distribution of the annealing process. A commercial 2-color pyrometer (Omega IR2C) system was also tested, but resulted in larger uncertainties in the actual temperature than simple “one-color” (intensity) measurements [32]. The camera used wavelengths between 3 and 5 μm. Since it can only record temperatures using a finite range, two ranges were used: (1) 310 °C – 890 °C, and (2) 630 °C – 1250°C. The thermal camera was calibrated using a heated 316L stainless steel plate with a type-K thermocouple welded to the surface. The plate was heated with a resistive ceramic heater while the camera recorded. Once the plate reached thermal equilibrium at some temperature, the emissivity value was adjusted until the camera and thermocouple readings were in good agreement. This was performed for dozens of temperatures from 300 °C to 1000 °C, such that both ranges described above were calibrated. An approximately linear change in emissivity with temperature was observed, so an effective emissivity of 0.4 was chosen as it lied in the middle of the measured emissivity range. This resulted in an approximate temperature measurement error of 25 °C (conservative estimate).

The furnace annealing was performed in a horizontal tube furnace in an inert (Ar) atmosphere while the bridges were still attached to the build plate. The furnace was brought up to temperature as quickly as possible (33 °C/min), held for the intended time, and cooled to room temperature over 3 h.

2.2. Characterization

The residual stress measurements were performed by measuring the deflection of the bridge after cutting through base of one bridge support. Using classic beam theory, the measured deflection can be used to calculate a linear stress profile that would have caused an equivalent amount of deformation using equation 1 [28],

$$\sigma = EL\frac{\partial^2 \nu}{\partial x^2} \tag{1}$$

where σ is the maximum stress, E is the elastic modulus (190 GPa for 316L stainless steel [11]), L is half the thickness of the bridge section, and ν is the measured deflection of the beam (bridge). The quantity $\partial^2\nu/\partial x^2$ is therefore the *curvature* of the beam deflection resulting from the support being cut (see Supporting Data, Fig. S2).

The stress profile calculated using Eq. (1) is not representative of the full residual stress state existing in the bridge (it is more complex than a linear profile). However, it is a measure for the magnitude of residual stress more tangible than the measured deflection, as it can be interpreted with respect to the yield stress. As such it will be referred to as the *released residual stress*. Although the deflection has been used as a substitute measurement for residual stress [20], the released residual stress can be used to account for variations in the bridge thicknesses and make direct comparisons between process parameters with a single numerical value.

To obtain the value of released residual stress, the surface profile of each bridge was measured before and after one support was cut using an optical microscope profile scanner (Keyence VR). The height profile was integrated over the width of the bridge, before and after the cut. The difference was used to calculate the deflection profile, which was fitted with a least-squares parabolic fit for the final calculation. The thickness of the overhang section was also determined by cutting off the bridge and measuring the underside height profile while correcting for the measured top surface (Fig. S3). The average thickness over the entire bridge section was then used in Eq. (1).

Electron back-scatter diffraction (EBSD) information was collected on a FEI XL-30 field-emission gun (FEG) scanning electron microscope (SEM) using an EDAX DigiView EBSD camera. Data processing and analysis were performed in EDAX OIM Analysis software. Optical microscope images were collected on an Olympus DSX510 with automatic stitching. Hardness data was collected on a Phase II, 900 − 391 Vickers microhardness tester using a 100 g (0.981 N) load with a 15 s dwell time. All microstructure data were collected after diamond sectioning, mechanical polishing, and electrolytic etching using 10% oxalic acid at 6 V for approximately 25 s.

3. Results

The released residual stresses measured after in situ annealing by the laser diodes are shown in Fig. 2a as a function of the diode power density input and compared to two furnace anneal processes (dashed lines). Each data point shown is the average of three separate bridges, with the error bars corresponding to one standard deviation (colored regions for the furnace anneals). The temperatures of both furnace heat treatments were chosen to mimic the peak temperatures that were measured for diode input powers at the onset of stress reduction and the maximum stress reduction. 4 min was chosen by using the rule-of-thumb, 1 h/inch of thickness for austenizing steel. Since residual stresses can decrease with increasing time at a certain temperature according to the Larson-Miller equation [15], (see Discussion) a heat

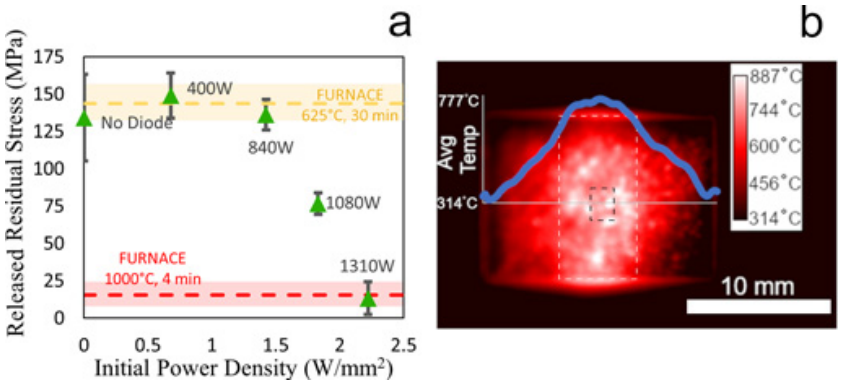

Fig. 2. a) Released residual stresses from the different experiments. Each data point is the average of 3 separate bridges built with the same conditions. Error bars shown are one standard deviation. The furnace annealed data (also measured from 3 separate bridges) is shown as dashed lines with the error bar shown as a colored band. b) Measured temperature of the diode annealing process (1.83 W/mm^2). The plot shows the average temperature, integrated vertically over the bridge. The black dotted line shows the location of the measurement area used for Fig. 3. The white dotted line shows the location of the bridge section. Note that the bridge is viewed at a 45° angle, so the length of the bridge appears shorter.

treatment duration of 30 min was chosen for the 625 °C anneal to increase the time at the maximum temperature by an order of magnitude compared to the in situ diode annealing.

The average released residual stress released by deformation after cutting through one support of the control bridge (which experienced no in situ annealing) was measured to be 134 ± 29 MPa (No Diode). In situ annealing with an initial surface power density up to 1.42 W/mm^2 did not reduce the released residual stress. This power density corresponded to a surface temperature of roughly 625 °C (Fig. 3). This temperature is approximate because the measured temperatures of the bridge overhang sections varied by about 75 °C from layer to layer due to fluctuations in surface roughness and residual heat from the scanning laser. In comparison, the furnace anneal performed at 625 °C for 30 min also showed no measurable decrease in residual stress. Above 1.42 W/mm^2, the released residual stress decreased with increasing diode energy input. At the maximum power density used in this work, 2.22 W/mm^2, the released residual stress was measured to be 13 ± 11 MPa, or approximately 10% of the measured residual stress in the control bridge. The peak temperature measured for this build was 1015 °C. Bridges furnace annealed at 1000 °C showed similar released residual stress (15 ± 7 MPa).

Although non-uniform temperatures can be expected even in a single block of material being heated by a uniform heat source (due to surface roughness and absorptivity variations), it is exacerbated in the bridges because of the varying thermal pathways that exist. The bridge supports have a better conductive pathway (vertically) to the build plate that acts as a heat sink and can therefore remain cooler than the overhang sections. The effect is seen in Fig. 2b. The temperatures shown in Fig. 3 were measured at z = 0.5 mm and 1.5 mm (i.e., at 10th and 30th layers, respectively), where z = 0 is the bottom of the overhang. Temperatures were averaged over a 2 x 2 mm area in the center of the overhang section (black dotted box, Fig. 2b). The cooling rate was approximately 50 °C/s during the power ramp-down period for the highest power in situ annealing (2.22 W/mm^2). The lower power annealing experiments showed slightly lower cooling rates due to the fixed power ramp-down rate.

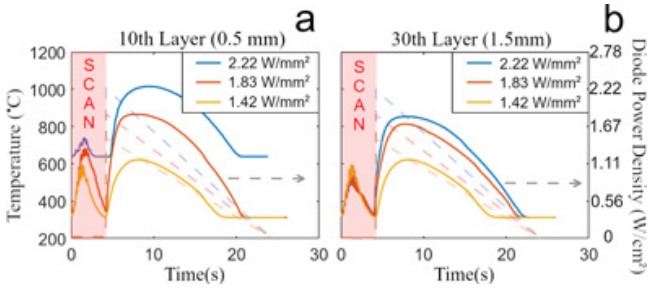

Fig. 3. The measured temperatures from the center (black dotted line in Fig. 2b) 2 x 2 mm of the bridges at a) 0.5 mm and b) 1.5 mm of thickness in the overhang section. The first peak is due to the passing melting laser. The dashed lines show the power density profile of the diode used in each experiment, plotted on the right axis. The error in the temperature measurement is approximately 25 °C (conservative estimate).

Table 1 shows the process parameters used for the different bridge builds. The surface energy density of the scanning laser (Power/[Speed * Hatch]) is close to that of the diode annealing laser, but the power density of the diode laser is orders of magnitude lower than the scanning laser (the focused scanning laser is approximately 5 × 10^5 J/mm^2). The listed annealing temperatures are estimated from the temperature measurements. Since the temperature of every layer could be not be measured (due to data bandwidth limitations), and substantial variability existed in the layer-to-layer temperature, only a temperature estimate could be made.

The decrease in residual stress was overwhelmingly due to recovery and not recrystallization. EBSD crystal orientation maps from bridges built without diode annealing, with 2.22 W/mm^2 diode annealing, and with a 1000 °C furnace anneal are shown, respectively, in Fig. 4a–c. No evidence of recrystallized grains or significant grain growth was observed; the grain size distributions from the three builds were comparable, with a mean equivalent grain diameter of approximately 9 μm (Fig. 4d). Grain growth or recrystallization would shift the grain size distributions to higher or lower values, respectively. A slight change in the grain size distributions could be seen comparing the “No Diode” and “Furnace, 1000 °C” bridges. Specifically, the number of small grains decreased slightly, concomitant with an increase in the number of grains with diameters near the mean value.

Optical and scanning electron microscope (SEM) images of the cross-sectioned bridges are shown in Fig. 5. The melt pool fusion boundaries and cellular-dendritic solidification cells are clearly visible with sharp boundaries in the build without the use of diode annealing. These solidification structures are typical of LPBF builds [33,34]. In contrast, the fusion boundaries and cellular-dendritic solidification structure are diminished in the furnace annealed (1000 °C) bridge due to chemical redistribution at elevated temperatures. In the 2.22 W/mm^2 diode-annealed bridge, the solidification cells are visible at the top of the build but diminish toward the bottom. Since the previously deposited layers (lower) were exposed to more diode annealing cycles than more recently-added layers (higher), these layers experience more time at the temperatures required for solute diffusion, leading to solidification substructures with less distinct boundaries. This is similar to the observed decomposition of the martensitic phase in only the lower layers of LPBF AM Ti6Al4V alloys [35].

Vicker’s microhardness measurements were also acquired along the bottom length of the bridge overhang sections (dotted red line in Fig. 6a). The average hardness without diode annealing was 260 ± 13 HV. For the bridges annealed in the furnace at 1000 °C, the average hardness dropped to roughly 205 ± 7 HV. The hardness of the 2.22 W/mm^2 diode-annealed bridge was measured along the top and bottom of the cross-section (dotted lines, Fig. 6a). As expected, the average hardness increased from 230 ± 13 HV at the bottom of the

Table 1
Laser process parameters used for the bridges and the annealing temperatures reached.

Process Laser Power (Scanning, Diode)	Scanning Laser Energy Density (J/mm^2)	Initial Diode Power Density (W/mm^2)	Diode Energy Density (J/mm^2)	Approximate Annealing Temperature (°C)
250 W, No Diode	9.09	0	0	–
250 W, 400W	9.09	0.68	6.78	350
250 W, 840W	9.09	1.42	14.24	625
250 W, 1080W	9.09	1.83	18.31	865
250 W, 1310W	9.09	2.22	22.21	1015
250 W, No Diode	9.09	0	0	625 (30 min)
250 W, No Diode	9.09	0	0	1000 (4 min)

overhang to 243 ± 13 HV at the top.

4. Discussion

4.1. Residual stress

Residual stress relaxation is affected by the temperature, hold time, and magnitude of the residual stress, which acts as a driving force for the process [14]. The experiments performed here attempted to remove the effects of the residual stress magnitude by keeping the laser melting conditions identical from bridge to bridge, thus keeping the as-deposited state of the residual stress roughly constant. The microstructure (and therefore mechanical properties) can also be affected from changes in the heat source or scanning strategy in addition to the

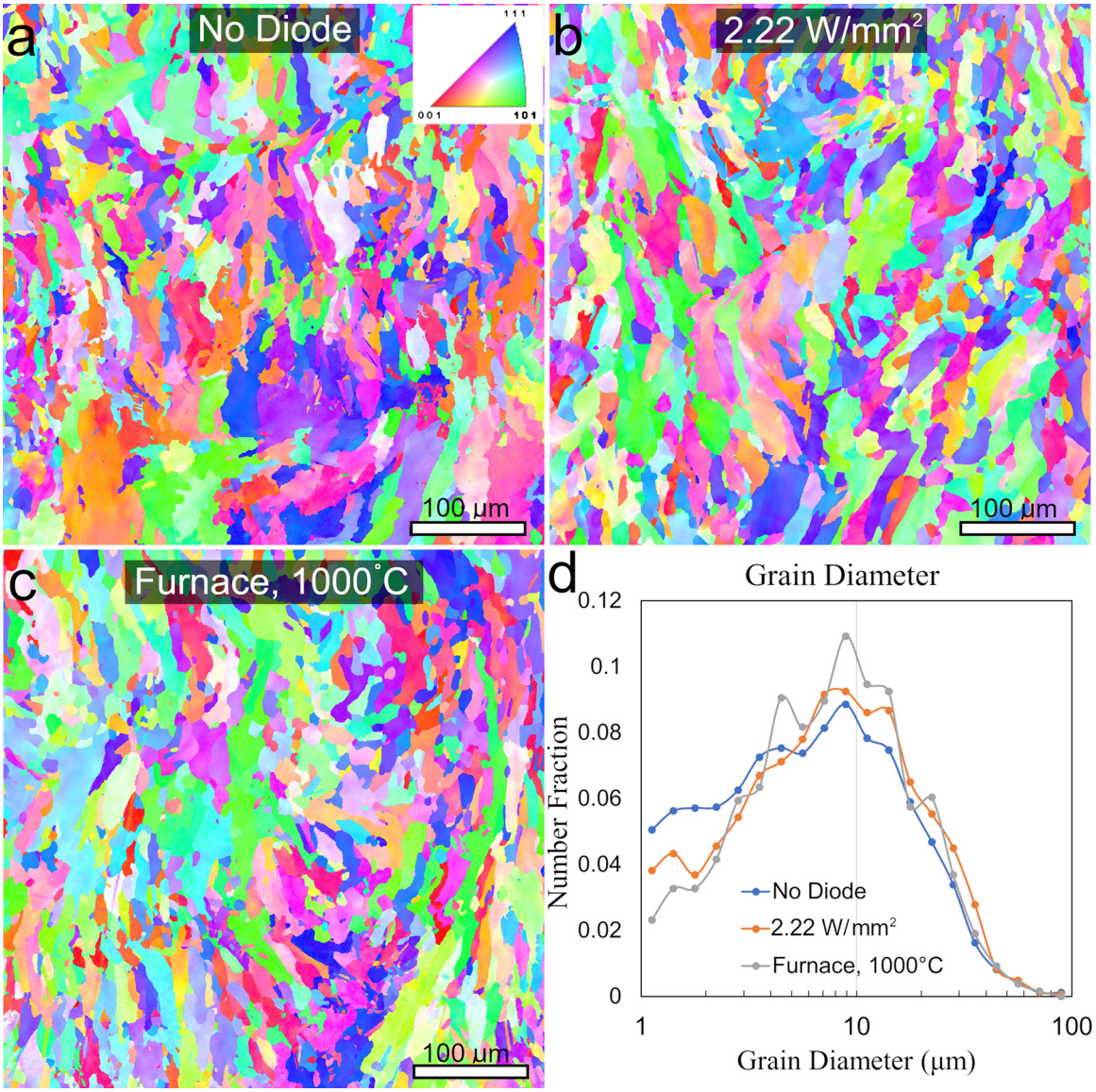

Fig. 4. Electron back-scatter diffraction crystal orientation maps of the a) No Diode, b) 2.22 W/mm^2 diode-annealed, and c) 1000 °C furnace-annealed bridges. d) The grain size distributions are comparable between the builds. The inset in a) shows the standard orientation triangle for an FCC material (the microstructure is comprised of austenitic stainless steel).

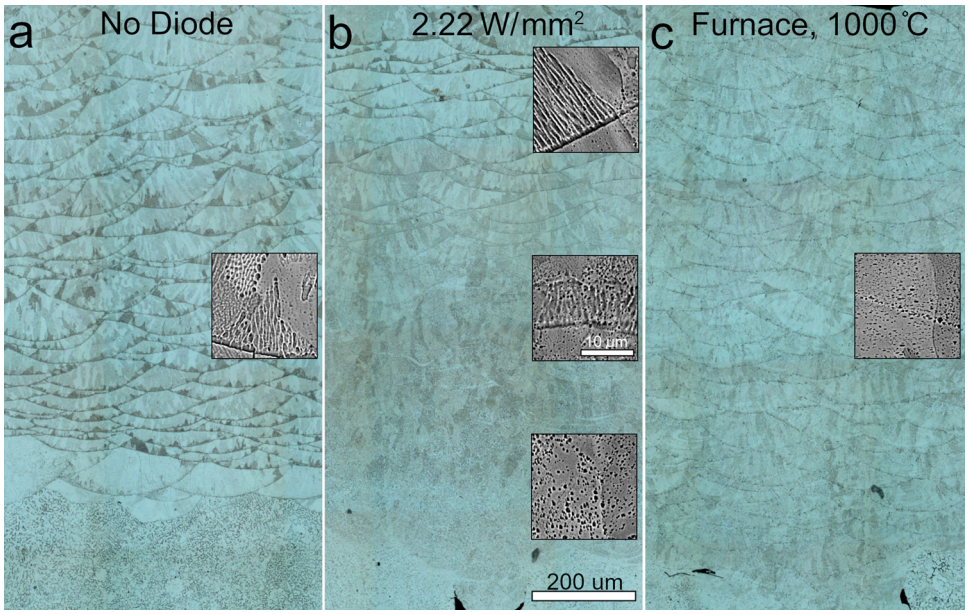

Fig. 5. a,b,c) Optical and SEM images (inset) of etched bridge cross-sections. The fusion boundaries are easily seen in the as-built (No Diode) bridge and fade when applying diode annealing or furnace annealing. The vertical placement of the inset images correspond to their physical location within the bridge. Scalebars in the optical and SEM images in b) apply to all optical and SEM images, respectively.

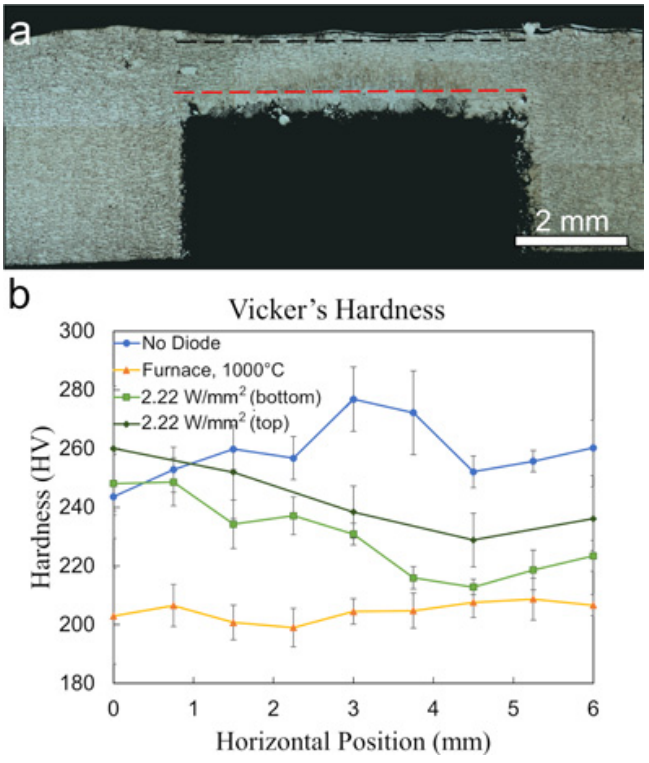

Fig. 6. a) Stitched optical image of a cross-sectioned diode-annealed bridge (2.22 W/mm^2) with locations of the hardness tested regions marked. Red shows the location taken in all three bridges, and black shows the upper location from the 2.22 W/mm^2 diode-annealed bridge. b) The average Vicker's hardness along the bridge section in the different bridge builds. The error bars shown are one standard deviation of the measured data (five data points) (For interpretation of the references to colour in this figure legend, the reader is referred to the web version of this article).

residual stress, which could affect the measurement of residual stress [13,33,36]. The consistent build strategy used here should mitigate changes in residual stress magnitude and microstructure and are therefore not considered; only the effects of time and temperature will be discussed.

The residual stress in bridges built with in situ diode annealing is clearly reduced above a critical temperature, while no changes were noticed for insufficiently high diode power input. The critical temperature was found to be above 625 °C. This finding correlates well with the yield stress of austenitic stainless steels, which decreases sharply above this temperature [37,38]. The residual stress relief correlates more strongly to the peak temperature reached than to the residence time at a particular temperature, as expected [14]. Dislocation annihilation and/or creep is the typical thermally-activated mechanism associated with the recovery process and can be described by the Larson-Miller equation given in Eq. (2)

$$Th = T(20 + log(t)) \quad (2)$$

where Th is a relative thermal effect (as Th increases, the residual stress decreases[2]), T is temperature in Kelvin, and t is time in hours [15]. The effect of temperature is much stronger than time in this relationship. For perspective, 5% increase in temperature has the same effect as a tenfold increase in holding time.

The importance of the maximum temperature reached was observed when comparing the furnace-annealed bridges (1000 °C) to the 2.22 W/mm^2 in situ diode-annealed bridges. The furnace-annealed bridges were heated from room temperature to 1000 °C at 33 °C/min (for a total ramp time of 30 min), held for 4 min, and ramped down to room temperature over 3 h. The peak temperature reached due to overshoot was approximately 1015 °C. The peak temperature of the 2.22 W/mm^2 diode anneal was also 1015 °C and the total time spent above 1000 °C was only several seconds per layer, for 25 layers total. The estimated time spent above 1000 °C was close to 90 s for the lowest layers, less for the upper layers. Comparing the furnace anneal to the in situ diode anneal, a threefold increase in time above 1000 °C did not decrease the residual stress any further.

The results suggest that a significant reduction in residual stress is possible by simply reaching the desired temperature. While diode annealing was applied to every layer (except for the first five layers of the overhang) in this study, less frequent in situ annealing steps could be comparably effective. A conservative approach was taken here to ensure the entire volume of material reached the desired temperature but the frequency of the in situ anneal could be reduced to skip multiple layers, given that the desired temperature could be still be reached in

[2] Th is the Larson-Miller Parameter, it traditionally is used to find the time and temperature to rupture by creep at a certain stress level [[39]], but can also describe residual stress relaxation [[15]].

unannealed underlying layers (a temperature decrease from the surface into underlying layers is unavoidable). This would significantly decrease the total build time, as each layer required an additional 20 s due to the diode heating. Additionally, the power ramp-down rate could be optimized. A faster cooling rate could still achieve lowered residual stress, but there could be a critical point at which increasing the cooling rate would introduce new thermal stresses and thus become the controlling factor in the final residual stress state. This is the subject of ongoing work.

4.2. Microstructure

Heating the AM bridges to temperatures above 1000 °C, whether by diode or furnace heating, did not result in significant grain growth or recrystallization. This is not unexpected, as additively manufactured metals have been shown to resist recrystallization to higher temperatures than wrought metals. This microstructural stability is attributed to the cellular solidification structure that is present in rapidly solidified metals [40]. The in situ annealing strategy leaves the cellular structure more intact than furnace annealing. This is evidenced by the SEM images of the bridges in Fig. 5. The cellular boundaries are less pronounced in the furnace-annealed bridge compared to the 2.22 W/mm^2 diode-annealed bridge. If the residual stresses could still be relieved with fewer in situ annealing treatments, the solidification cellular microstructure could be better preserved.

Hardness is known to correlate with dislocation density and residual stress [41–43]. Hardness is also correlated to finer solidification structures, and the chemical segregation that forms dislocations in cell walls [34,44]. The hardness distribution in the bridges follows the expectation of higher hardness with more chemical segregation/dislocation density: the furnace-annealed bridge retains the least solute segregation in the cell walls while the diode-annealed bridge retains slightly more solute segregation in the cell walls. In the diode-annealed bridge, solute segregation is better preserved in regions that experienced fewer annealing cycles (i.e., at the top of the bridge).

Despite the temperature variation over the bridge overhang section during in situ annealing (Fig. 2b), the hardness of the 2.22 W/mm^2 diode-annealed bridge did not vary greatly from the middle to the edge of the overhang. The variation was similar to that of the un-annealed (No Diode) bridge. This implies the temperature distribution does not need to be highly uniform to achieve reasonable residual stress reduction. Better uniformity of the temperature distribution could be achieved using the setup described by Matthews et al. [30] wherein an optically addressable light valve was used to locally shape the intensity profile. Scaling the intensity over the part could achieve a more uniform temperature. This approach or another means to fluidly control the annealing laser intensity would also be useful for more complex parts with disparate feature sizes or changing cross-section as the part builds. Intensity shaping will likely be necessary in an industrial setting because of the vast number of geometries amenable to manufacture by LPBF, but it will make direct production of nearly stress-free LPBF parts possible.

5. Conclusion

Residual stress control by in situ diode annealing in a laser powder-bed fusion process was successfully demonstrated. By controlling the surface temperature of the material in situ, residual stresses can be effectively reduced *during* additive manufacturing. A residual stress reduction of 90% was realized in 316 L stainless steel bridge structures without grain growth or recrystallization, and with only minor changes to the solidification structure. The peak temperature reached during annealing was found to have a much greater effect than the dwell time at the annealing temperature. Further improvements can be made by optimizing the frequency of the in situ diode annealing process (i.e., number of layers per heating cycle), the ramp rates of the power profile, and the spatial distribution of the diode light intensity. This method could prove useful for decreasing risk during LPBF by directly manufacturing near stress-free parts regardless of height and removes the need for stress-relieving post processing.

Acknowledgements

This work was performed under the auspices of the U.S. Department of Energy, by Lawrence Livermore National Laboratory (LLNL) under Contract No. DE-AC52-07NA27344. This work was supported through the LLNL Laboratory Directed Research and Development Program under project tracking code 18-SI-003.

Appendix A. Supplementary data

Supplementary material including density measurements as a function of scanning laser parameters, a description of the residual stress measurement process, and a thermal and optical video of the build process (1.42 W/mm^2 in situ anneal) can be found in the online version, at doi:https://doi.org/10.1016/j.addma.2019.05.009.

References

[1] W.E. King, A.T. Anderson, R.M. Ferencz, N.E. Hodge, C. Kamath, S.A. Khairallah, A.M. Rubenchik, Laser powder bed fusion additive manufacturing of metals; Physics, computational, and materials challenges, Appl. Phys. Rev. 2 (2015) 041304, , https://doi.org/10.1063/1.4937809.
[2] W.E. Frazier, Metal additive manufacturing: a review, J. Mater. Eng. Perform. 23 (2014) 1917–1928, https://doi.org/10.1007/s11665-014-0958-z.
[3] G. Tapia, A. Elwany, A review on process monitoring and control in metal-based additive manufacturing, J. Manuf. Sci. Eng. 136 (2014), https://doi.org/10.1115/1.4028540 060801-060801–10.
[4] P.J. DePond, G. Guss, S. Ly, N.P. Calta, D. Deane, S. Khairallah, M.J. Matthews, In situ measurements of layer roughness during laser powder bed fusion additive manufacturing using low coherence scanning interferometry, Mater. Des. 154 (2018) 347–359, https://doi.org/10.1016/j.matdes.2018.05.050.
[5] N.P. Calta, J. Wang, A.M. Kiss, A.A. Martin, P.J. Depond, G.M. Guss, V. Thampy, A.Y. Fong, J.N. Weker, K.H. Stone, C.J. Tassone, M.J. Kramer, M.F. Toney, A.V. Buuren, M.J. Matthews, An instrument for in situ time-resolved X-ray imaging and diffraction of laser powder bed fusion additive manufacturing processes, Rev. Sci. Instrum. 89 (2018) 055101, , https://doi.org/10.1063/1.5017236.
[6] M.J. Matthews, G. Guss, S.A. Khairallah, A.M. Rubenchik, P.J. Depond, W.E. King, Denudation of metal powder layers in laser powder bed fusion processes, Acta Mater. 114 (2016) 33–42, https://doi.org/10.1016/j.actamat.2016.05.017.
[7] C. Li, Z.Y. Liu, X.Y. Fang, Y.B. Guo, Residual stress in metal additive manufacturing, Proc. CIRP 71 (2018) 348–353, https://doi.org/10.1016/j.procir.2018.05.039.
[8] M. Strantza, R.K. Ganeriwala, B. Clausen, T.Q. Phan, L.E. Levine, D. Pagan, W.E. King, N.E. Hodge, D.W. Brown, Coupled experimental and computational study of residual stresses in additively manufactured Ti-6Al-4V components, Mater. Lett. 231 (2018) 221–224, https://doi.org/10.1016/j.matlet.2018.07.141.
[9] B. Vrancken, Study of Residual Stresses in Selective Laser Melting, (2016) (Accessed 17 December 2018), https://lirias.kuleuven.be/retrieve/391175.
[10] H. Ali, L. Ma, H. Ghadbeigi, K. Mumtaz, In-situ residual stress reduction, martensitic decomposition and mechanical properties enhancement through high temperature powder bed pre-heating of selective laser melted Ti6Al4V, Mater. Sci. Eng. A 695 (2017) 211–220, https://doi.org/10.1016/j.msea.2017.04.033.
[11] A.S. Wu, D.W. Brown, M. Kumar, G.F. Gallegos, W.E. King, An experimental investigation into additive manufacturing-induced residual stresses in 316L stainless steel, Metall. Mater. Trans. A 45 (2014) 6260–6270, https://doi.org/10.1007/s11661-014-2549-x.
[12] C. Li, J.F. Liu, Y.B. Guo, Prediction of residual stress and part distortion in selective laser melting, Proc. CIRP 45 (2016) 171–174, https://doi.org/10.1016/j.procir.2016.02.058.
[13] P. Mercelis, J.-P. Kruth, Residual stresses in selective laser sintering and selective laser melting, Rapid Prototyp. J. (2013), https://doi.org/10.1108/13552540610707013.
[14] G.E. Totten, M. Howes, T. Inoue, Stability of residual stress, Handb. Residual Stress Deform. Steel, ASM International, 2002, pp. 54–69.
[15] D.A. Canonico, Stress-relief heat treating of steel, ASM Handb. Vol. 4A Steel Heat Treat. Fundam. Process, 1st ed., ASM International, 1991, pp. 33–34.
[16] M.R. James, Relaxation of residual stresses an overview, Pergamon Press Adv. Surf. Treat. Technol. Appl.Eff. 4 (1987) 349–365.
[17] G. Vastola, G. Zhang, Q.X. Pei, Y.-W. Zhang, Active control of microstructure in powder-bed fusion additive manufacturing of Ti6Al4V, Adv. Eng. Mater. 19 (2017) 1700333, https://doi.org/10.1002/adem.201700333.
[18] A. Vasinonta, J.L. Beuth, M. Griffith, Process maps for predicting residual stress and melt Pool size in the laser-based fabrication of thin-walled structures, J. Manuf. Sci. Eng. 129 (2006) 101–109, https://doi.org/10.1115/1.2335852.
[19] P. Aggarangsi, J. Beuth, Localized preheating approaches for reducing residual

stress in additive manufacturing, Department of Mechanical Engineering Carnegie Mellon University Pittsburgh, PA, Pittsburgh, PA, 2006, pp. 709–720.
[20] D. Buchbinder, W. Meiners, N. Pirch, K. Wissenbach, J. Schrage, Investigation on reducing distortion by preheating during manufacture of aluminum components using selective laser melting, J. Laser Appl. 26 (2013) 012004, , https://doi.org/10.2351/1.4828755.
[21] M.B. Prime, M.R. Hill, A.T. DeWald, R.J. Sebring, D.R. Vivek, M.J. Cola, Residual stress mapping in welds using the contour method, Proc. 6th Int. Conf. (2002) 891–896.
[22] W. Woo, G.B. An, E.J. Kingston, A.T. DeWald, D.J. Smith, M.R. Hill, Through-thickness distributions of residual stresses in two extreme heat-input thick welds: a neutron diffraction, contour method and deep hole drilling study, Acta Mater. 61 (2013) 3564–3574, https://doi.org/10.1016/j.actamat.2013.02.034.
[23] M. Strantza, B. Vrancken, M.B. Prime, C.E. Truman, M. Rombouts, D.W. Brown, P. Guillaume, D. Van Hemelrijck, Directional and oscillating residual stress on the mesoscale in additively manufactured Ti-6Al-4V, Acta Mater. 168 (2019) 299–308, https://doi.org/10.1016/j.actamat.2019.01.050.
[24] B. Vrancken, V. Cain, R. Knutsen, J. Van Humbeeck, Residual stress via the contour method in compact tension specimens produced via selective laser melting, Scr. Mater. 87 (2014) 29–32, https://doi.org/10.1016/j.scriptamat.2014.05.016.
[25] B. Vrancken, S. Buls, J.-P. Kruth, J.V. Humbeeck, Preheating of selective laser melted Ti6Al4V: microstructure and mechanical properties, Proc. 13th World Conf. Titan. (2016) 1269–1277, https://doi.org/10.1002/9781119296126 ch215..
[26] J.L. Bartlett, B.P. Croom, J. Burdick, D. Henkel, X. Li, Revealing mechanisms of residual stress development in additive manufacturing via digital image correlation, Addit. Manuf. 22 (2018) 1–12, https://doi.org/10.1016/j.addma.2018.04.025.
[27] R.K. Ganeriwala, M. Strantza, W.E. King, B. Clausen, T.Q. Phan, L.E. Levine, D.W. Brown, N.E. Hodge, Evaluation of a thermomechanical model for prediction of residualstress during laser powder bed fusion of Ti-6Al-4V, Addit. Manuf. (2019), https://doi.org/10.1016/j.addma.2019.03.034.
[28] J.-P. Kruth, J. Deckers, E. Yasa, R. Wauthlé, Assessing and comparing influencing factors of residual stresses in selective laser melting using a novel analysis method, Proc. Inst. Mech. Eng. Part B J. Eng. Manuf. 226 (2012) 980–991, https://doi.org/10.1177/0954405412437085.
[29] S.A. Sillars, C.J. Sutcliffe, A.M. Philo, S.G.R. Brown, J. Sienz, N.P. Lavery, The three-prong method: a novel assessment of residual stress in laser powder bed fusion, Virtual Phys. Prototyp. 13 (2018) 20–25, https://doi.org/10.1080/17452759.2017.1392682.
[30] M.J. Matthews, G. Guss, D.R. Drachenberg, J.A. Demuth, J.E. Heebner, E.B. Duoss, J.D. Kuntz, C.M. Spadaccini, Diode-based additive manufacturing of metals using an optically-addressable light valve, Opt. Express. 25 (2017) 11788–11800, https://doi.org/10.1364/OE.25.011788.
[31] R. Mertens, S. Clijsters, K. Kempen, J.-P. Kruth, Optimization of scan strategies in selective laser melting of aluminum parts with downfacing areas, J. Manuf. Sci. Eng. 136 (2014), https://doi.org/10.1115/1.4028620 061012-061012–7.
[32] M. Virgo, K.J. Quigley, S. Chemerisov, G.F. Vandegrift, Low-Cost, High-Performance Alternatives for Target Temperature Monitoring Using the Near-Infrared Spectrum, Argonne National Laboratory (ANL), Argonne, IL (United States), 2017.
[33] T.T. Roehling, S.S.Q. Wu, S.A. Khairallah, J.D. Roehling, S.S. Soezeri, M.F. Crumb, M.J. Matthews, Modulating laser intensity profile ellipticity for microstructural control during metal additive manufacturing, Acta Mater. 128 (2017) 197–206, https://doi.org/10.1016/j.actamat.2017.02.025.
[34] Y.M. Wang, T. Voisin, J.T. McKeown, J. Ye, N.P. Calta, Z. Li, Z. Zeng, Y. Zhang, W. Chen, T.T. Roehling, R.T. Ott, M.K. Santala, P.J. Depond, M.J. Matthews, A.V. Hamza, T. Zhu, Additively manufactured hierarchical stainless steels with high strength and ductility, Nat. Mater. 17 (2018) 63–71, https://doi.org/10.1038/nmat5021.
[35] W. Xu, M. Brandt, S. Sun, J. Elambasseril, Q. Liu, K. Latham, K. Xia, M. Qian, Additive manufacturing of strong and ductile Ti–6Al–4V by selective laser melting via in situ martensite decomposition, Acta Mater. 85 (2015) 74–84, https://doi.org/10.1016/j.actamat.2014.11.028.
[36] R. Dehoff, M. Kirka, W. Sames, H. Bilheux, A. Tremsin, L. Lowe, S. Babu, Site specific control of crystallographic grain orientation through electron beam additive manufacturing, Mater. Sci. Technol. 31 (2015) 931–938, https://doi.org/10.1179/1743284714Y.0000000734.
[37] D.A. Canonico, Stress-relief heat treating of steel, ASM Handb. Vol 4 Heat Treat, ASM International, 1991.
[38] Long Products Stainless Steel Grade Sheet, 316316L - North Am. Stainl, (2018) https://www.northamericanstainless.com/wp-content/uploads/…/Grade-316-316L1.pdf (accessed December 20, 2018).
[39] J.G. Kaufman, Parametric Analyses of High-Temperature Data for Aluminum Alloys, ASM International, Materials Park, OH, 2008.
[40] T.R. Smith, J.D. Sugar, J.M. Schoenung, C. San Marchi, Anomalous annealing response of directed energy deposited type 304L austenitic stainless steel, JOM. 70 (2018) 358–363, https://doi.org/10.1007/s11837-017-2711-1.
[41] S.C. Schroeder, J. Frankel, A. Abbate, The Relationship between Residual Stress and Hardness and the Onset of Plastic Deformation., ARMY ARMAMENT RESEARCH DEVELOPMENT AND ENGINEERING CENTER WATERVLIET NY BENET LABS, (1995) (accessed December 17, 2018), https://apps.dtic.mil/docs/citations/ADA302173.
[42] M. Odnobokova, A. Kipelova, A. Belyakov, R. Kaibyshev, Microstructure evolution in a 316L stainless steel subjected to multidirectional forging and unidirectional bar rolling, IOP Conf. Ser. Mater. Sci. Eng. 63 (2014) 012060, , https://doi.org/10.1088/1757-899X/63/1/012060.
[43] K. Tosha, Influence of Residual Stresses on the Harndess Number in the Affected Layer Produced by Shot Peening, Shotpeener.Com, Seoul, South Korea, 2002 (accessed December 17, 2018), https://www.shotpeener.com/library/detail.php?anc=1990059&keyword=influence+of+residual+stress+hardness.
[44] Q. Jia, D. Gu, Selective laser melting additive manufacturing of inconel 718 superalloy parts: densification, microstructure and properties, J. Alloys Compd. 585 (2014) 713–721, https://doi.org/10.1016/j.jallcom.2013.09.171.